

Nanopore Formation in a Polyphenylene Low-*k* DielectricMichael S. Silverstein\*<sup>†</sup> and Michal Shach-Caplan

Department of Materials Engineering, Technion—Israel Institute of Technology, Haifa 32000, Israel

Barry J. Bauer,\* Ronald C. Hedden,<sup>‡</sup> and Hae-Jeong Lee

Polymers Division, National Institute of Standards and Technology, Gaithersburg, Maryland 20899

Brian G. Landes

Dow Chemical Company, Midland, Michigan 48674

Received December 22, 2004; Revised Manuscript Received March 13, 2005

**ABSTRACT:** Nanometer-scale porosity is being introduced into low-*k* dielectrics in an attempt to achieve inter-level metal insulators with permittivities less than 2.0. It has proven extremely difficult to describe pore formation and to characterize the porous structure. This work investigates pore formation in a polyphenylene low-*k* dielectric based on pyrolysis of a porogen (27 vol %) in a polyphenylene matrix. One unique aspect presented here is the characterization of the nanoscale structure at various stages of pore formation through the use of a deuterated porogen. The combination of X-ray reflectivity (XRR) and small-angle neutron scattering (SANS) is found to be a powerful technique for describing porogen degradation and pore formation in nanoporous materials. The average radius of the porogen domains was approximately 60 Å with a relatively broad size distribution. During degradation the smaller porogen domains collapse, while the larger domains yield stable pores. This collapse of the relatively large number of smaller domains results in a significant reduction in film thickness, a porosity that is significantly smaller than the porogen content, a pore size distribution that is narrower than the porogen domain size distribution, and an average pore size of approximately 80 Å.

**Introduction**

The demand for increased signal transmission speed and device density in the next generation of multilevel integrated circuits has placed stringent demands on materials performance. The *International Technology Roadmap for Semiconductors, 2004 Update* indicates that permittivities of less than 2.0 will be required for interlevel metal insulators in the future.<sup>1</sup> Nanometer-scale porosity is being introduced into low-*k* dielectrics in an attempt to achieve such low permittivities. Introducing tiny, air-filled pores lowers the dielectric constant of the material, but also perturbs mechanical, thermal and barrier properties of the films. To facilitate development of low-*k* materials with optimal properties, the pore structure must be characterized. However, it has proved extremely difficult to describe the mechanism of pore formation and to characterize the porous structure (porosity, pore size, pore size distribution) owing to the nanometer scale of the pores.

The combination of X-ray reflectivity (XRR) and small-angle neutron scattering (SANS) has been demonstrated to be a powerful technique for describing the porosity and nanoscale architecture of nanoporous low-*k* thin films.<sup>2–7</sup> The techniques that have been used to investigate the pore size distribution in nanoporous low-*k* materials include ellipsometric porosimetry,<sup>8–13</sup> XRR porosimetry,<sup>14–16</sup> SANS porosimetry,<sup>17–20</sup> positronium annihilation lifetime spectroscopy (PALS),<sup>21–23</sup> small-angle X-ray scattering (SAXS)<sup>24,25</sup> and neutron reflectivity.<sup>26</sup> Ellipsometry, XRR, and PALS have been used to characterize a set of samples, yielding similar

pore sizes, and the advantages and disadvantages of the different techniques have been discussed.<sup>11,27</sup> The wide range of materials under consideration for low-*k* dielectrics include spin-on deposited polyphenylenes,<sup>28</sup> poly(arylene ethers),<sup>16</sup> and hydrogen or methyl silsesquioxanes<sup>14,21</sup> as well as plasma-enhanced chemical-vapor-deposited (PECVD) carbon-doped silicon oxide (SiOCH).<sup>9,14,29</sup> The methods for incorporating the porogen in the spin-on materials vary from simple mixtures<sup>21</sup> to block copolymer templates.<sup>23,30</sup> The materials under consideration and the characterization techniques being developed to determine their structures and properties have been described in recent reviews.<sup>31,32</sup>

This work investigates pore formation in a polyphenylene low-*k* dielectric based on pyrolysis of a porogen in a polyphenylene oligomer matrix.<sup>33</sup> Several techniques, such as ellipsometry and small-angle X-ray scattering, have been used to characterize such materials.<sup>34,35</sup> One unique aspect of this research is the description of the nanoscale structure at various stages of pore formation through the use of a deuterated porogen. The use of a deuterated porogen provides exceptional neutron scattering contrast in the porogen-oligomer system. Thus, SANS from the porogen-oligomer system before cure can be compared to SANS from the porous polymer system after cure.

**Experimental Section**

**Materials.** Certain commercial equipment and materials are identified in this paper in order to specify adequately the experimental procedure. In no case does such identification imply recommendation by NIST nor does it imply that the material or equipment identified is necessarily the best available for this purpose.

The porous organic low-*k* material investigated in this research is based on a developmental version (V7) of Dow

\* Corresponding author.

<sup>†</sup> E-mail: michaelst@tx.technion.ac.il.<sup>‡</sup> Present address: Department of Materials Science and Engineering, Penn State University, University Park, PA 16802.

**Table 1. Atomic Composition, Density and Calculated Neutron Scattering Length Density<sup>a</sup>**

	C, mass %	H, mass %	D, mass %	O, mass %	<i>d</i> , g/cm <sup>3</sup>	SLD, Å <sup>-2</sup> × 10 <sup>6</sup>
oligomer	93.16	5.04	0	1.80	1.18	2.37
polymer	93.48	5.07	0	1.45	1.18	2.37
porogen	86.34	0.74	12.92	0	1.07	5.67
calculated: 75/25 oligomer/porogen	91.46	3.96	3.23	1.35	1.15	

<sup>a</sup> Uncertainties are discussed in the text.

**Table 2. Processing Conditions and Ellipsometry Results<sup>a</sup>**

sample	cure, °C	expected porogen degradation, %	<i>t</i> , μm	<i>s</i> , %	<i>n</i>	<i>p<sub>n</sub></i> , %
150A		0	1.215		1.6329	
150B		0	1.505		1.6294	
330A	330	0	1.210	0.4	1.6239	1.1
330B	330	0	1.515	-0.7	1.6256	0.5
400A	400	≈50	1.095	9.9	1.6226	1.3
400B	400	≈50	1.29	16.4	1.6249	0.6
430A	430	100	0.995	18.1	1.5838	6.3
430B	430	100	1.205	19.9	1.5994	3.9
43040A	430 <sup>b</sup>	100	0.935	23.1	1.5981	4.4
43040B	430 <sup>b</sup>	100	1.15	23.6	1.6099	2.5

<sup>a</sup> Uncertainties are discussed in the text. <sup>b</sup> Held for 40 min.

Chemical's SiLK polyphenylene precursor especially prepared for this work. The deuterated polymeric porogen (hereafter referred to as the porogen) yields neutron scattering contrast in the porogen-oligomer system. The densities of the low-*k* cross-linked polymeric matrix (the oligomer following a complete cure, hereafter referred to as the polymer) and the porogen are (1.18 and 1.07) g/cm<sup>3</sup>, respectively. The mass fractions of C, H, D, and O for the oligomer, the polymer, and the porogen are listed in Table 1. The mass fractions of C, H, D, and O for a mixture of oligomer and porogen with a 75:25 oligomer to porogen mass ratio (73.1:26.9 volume ratio) are also listed in Table 1.

The films were prepared by spin-casting a porogen-filled oligomer and subsequently baking at 150 °C. Two sets of samples were prepared; set A was baked at 150 °C for 24 h, while set B was baked at 150 °C for 48 h. Films at various stages of porogen degradation were investigated (Table 2). Previous experience with the thermal degradation of the porogen indicates that porogen degradation is incomplete following a cure at 400 °C, while porogen degradation is complete following a cure at 430 °C. The films were not held at the cure temperature unless otherwise noted. The sample names in Table 2 reflect the processing (the maximum temperature that was reached during processing followed by the cure hold time in minutes (if applicable) and the bake process (A or B)).

**Characterization.** Ellipsometry was used to provide an initial estimate for the film thickness and porosity. Fourier transform infrared spectroscopy (FTIR) was performed in reflection from (500 to 4000) cm<sup>-1</sup> at a resolution of 2 cm<sup>-1</sup> (Bruker Equinox 55). The peaks at (2360 and 2330) cm<sup>-1</sup> in the FTIR spectra represent CO<sub>2</sub> from the surroundings. X-ray photoelectron spectroscopy (XPS) was performed using a low resolution scan for elemental composition and a high-resolution scan for the C<sub>1s</sub> and O<sub>1s</sub> spectra (Thermo Sigma Probe, VG Scientific). The uncertainty in the elemental composition from XPS, based on previous experience with repeated measurements, is 10% of the calculated atomic fraction. The C-C peak was shifted to a binding energy of 285.0 eV, and the peak fitting was done using the built-in software. High-resolution scanning electron microscopy (HRSEM) of the film surfaces was performed on uncoated specimens using accelerating voltages from 1 to 3 kV (LEO 982, Zeiss).

**Specular X-ray Reflectivity.** Specular X-ray reflectivity measurements (XRR) were performed using a modified Philips high-resolution X-ray diffractometer equipped with an environmental control chamber with Be windows. Data were

collected at the specular condition, with the grazing incident angle,  $\theta_i$ , equal to the detector angle  $\theta_d$ . The reflected intensity was recorded as a function of angle. XRR measurements were performed both under vacuum and in the presence of saturated solvent vapors, which condense in the pores. Both methanol and toluene were used as adsorbents, since they were expected to have quite different solubilities in the film. The magnitude of the X-ray momentum transfer in the film thickness direction,  $q_z$ , is related to  $\theta_i$  and the wavelength of the Cu K $\alpha_1$  radiation (1.54 Å),  $\lambda_X$ , by  $q_z = (4\pi \sin \theta_i)/\lambda_X$ . The data were plotted as the log of the relative intensity (reflected beam intensity,  $I$ , divided by the incident beam intensity,  $I_0$ ) vs  $q_z$ . The average electron densities of the films were deduced using a computer modeling routine (*m-layer*) capable of simulating reflectivity from multilayer structures.<sup>36</sup>

**Small-Angle Neutron Scattering.** The homogeneous materials in this work, the oligomer, polymer, and porogen, can each be described by a neutron scattering length density (SLD). The SLD of component  $i$  is  $\rho_i \sigma_i$ , where  $\rho_i$  is its mass density and  $\sigma_i$  is the total scattering length per unit mass defined by<sup>17</sup>

$$\sigma_i = \frac{N_A \sum_j c_j b_j}{\sum_j c_j m_j} \quad (1)$$

where  $c_j$  is the local molar concentration of a nucleus  $j$ ,  $b_j$  is its scattering length,  $m_j$  is its molar mass, and  $N_A$  is Avogadro's number. The densities and compositions in Table 1 were used to calculate the neutron scattering length densities (the oligomer density was assumed to be identical to that of the polymer, 1.18 g/cm<sup>3</sup>). The resulting SLDs were  $2.37 \times 10^{-6}$  Å<sup>-2</sup> for the oligomer and polymer and  $5.67 \times 10^{-6}$  Å<sup>-2</sup> for the porogen.

The scattering contrast between two materials is defined as the difference between their SLDs. The porogen-oligomer contrast is therefore  $3.30 \times 10^{-6}$  Å<sup>-2</sup>, greater than the polymer-pore contrast of  $2.37 \times 10^{-6}$  Å<sup>-2</sup>. For a two phase blend in which each phase has a homogeneous atomic composition, the scattered intensity,  $I(q)$ , is proportional to the contrast between the two phases squared, regardless of sample morphology:<sup>17</sup>

$$I(q) \propto (\rho_1 \sigma_1 - \rho_2 \sigma_2)^2 \quad (2)$$

where  $q$  is the scattering vector, related to the scattering angle,  $2\theta_s$ , and the neutron wavelength,  $\lambda_N$ , by  $q = (4\pi \sin \theta_s)/\lambda_N$ .

Small-angle neutron scattering (SANS) was performed on the 8 m NG1 instrument, with a wavelength spread of 12% and the 30 m NG7 instrument, with a wavelength spread of 11%, at the National Institute of Standards and Technology (NIST) Center for Neutron Research. The high  $q$  range SANS data (0.013–0.091 Å<sup>-1</sup>) were taken on the 8 m SANS using a wavelength of 6 Å, the mid-range data (0.005–0.051 Å<sup>-1</sup>) were taken on the 8 m SANS using a wavelength of 12 Å and the low-range data (0.002–0.027 Å<sup>-1</sup>) were taken on the 30 m SANS using a wavelength of 6 Å. The data are plotted as intensity vs  $q$  on a log-log scale. Fits of the scattering data were made by a least-squares fit, giving an average and a standard deviation to the fit.

The relative uncertainties of the data presented are estimated as one standard deviation of the mean. The total combined uncertainties from all external sources are not reported, as comparisons are made with data obtained under the same conditions. In cases where the limits are smaller than

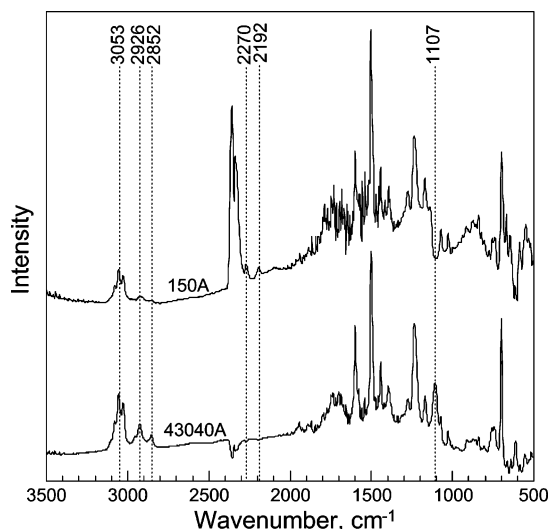


**Figure 1.** FTIR spectra from 150A and 43040A.

the plotted symbols, the limits are left out for clarity. All temperatures reported are within  $\pm 1$  °C, thicknesses are within  $\pm 1$  nm,  $q_e^2$  within  $\pm 1 \times 10^{-5}$  Å<sup>-2</sup>, and densities and porosities within  $\pm 3\%$ , as determined by the previous experience of repeated measurements. The standard deviations from the fits of the SANS data using a polydisperse hard sphere model were less than  $\pm 2\%$  for radius,  $\pm 3\%$  for polydispersity, and  $\pm 0.5\%$  for scattering contrast.

## Results and Discussion

**Molecular Structure and Morphology.** The cross-linked polyphenylene matrix is formed through the reaction of polyfunctional cyclopentadienone- and acetylene-substituted monomers, liberating CO.<sup>28</sup> There are two simultaneous processes occurring on exposure of the porogen-filled oligomer to elevated temperatures, the formation of a cross-linked polyphenylene matrix and the degradation of the porogen. The similarities in the FTIR spectra from the porogen-filled oligomer (150A) and from the porous polymer (43040A) in Figure 1 stem from the common bands associated with the aromatic groups, the cyclopentadienone, and the silicon substrate that are present in both samples. There are, however, several significant differences between the two FTIR spectra. The bands representing acetylene groups at 2192 and 2270  $\text{cm}^{-1}$  are present in 150A but not in 43040A. The disappearance of the acetylene groups indicates that they have cross-linked during cure, as expected. In addition, the FTIR spectrum for 43040A exhibits bands at 2926 and 2852  $\text{cm}^{-1}$  that are not as significant in the spectrum for 150A. These bands are associated with methyl and methylene groups. The FTIR spectrum for 43040A also exhibits a band at 1107  $\text{cm}^{-1}$  that was not present in the spectrum for 150A. This band is associated with an aliphatic ether. These bands in 43040A indicate the presence of an ether-containing hydrocarbon. This hydrocarbon is most likely a residue from the degradation of the porogen in the presence of the CO liberated in the curing reaction. The FTIR bands around 2350  $\text{cm}^{-1}$  in Figure 1 represent CO<sub>2</sub> in the spectrometer environment and do not originate in the samples.

The changes in molecular structure observed through FTIR are confirmed by atomic composition and structural data from XPS. The atomic percent of oxygen present in 150A, 3.5%, increases to 4.0% in 400A, and to 7.0% in 43040A. As seen in Figure 2, the O<sub>1s</sub> spectra

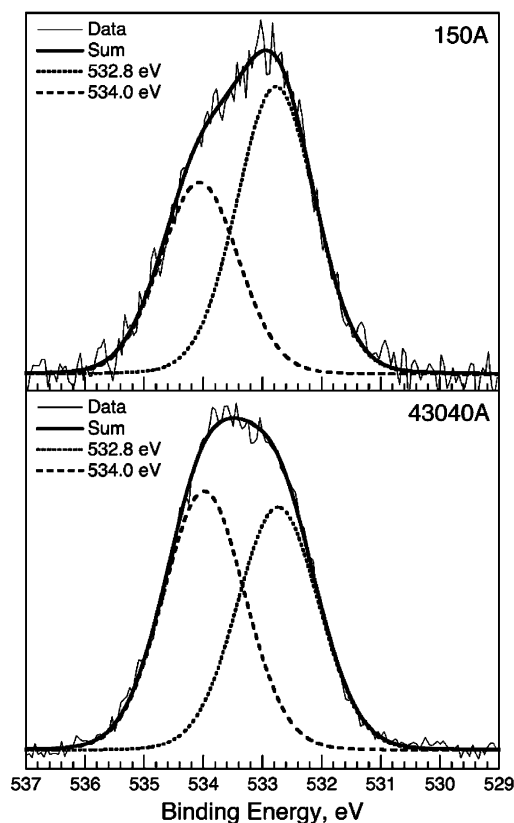


**Figure 2.** O<sub>1s</sub> XPS spectra from 150A and 43040A.

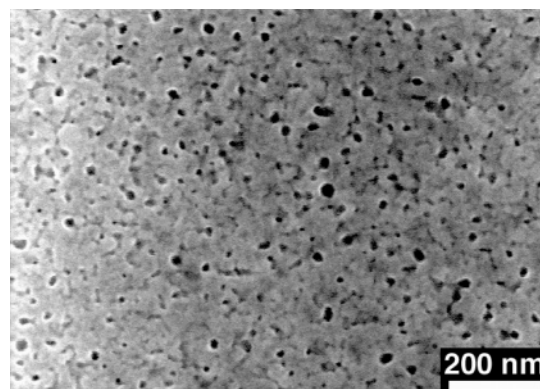


**Figure 3.** HRSEM micrograph of 43040A surface.

can be divided into two peaks, one at 532.8 eV representing an aromatic carbonyl and one at 534.0 eV representing an aromatic ether or aromatic hydroxyl. While approximately 64% of the oxygen is aromatic carbonyl for 150A, this amount is reduced to approximately 48% for 400A and 43040A. The increase in the amount of oxygen, and, specifically, in the oxygen associated with an aromatic ether or hydroxyl may also indicate the presence of residue from the degradation of the porogen during the curing process. Such changes in the molecular structure have not been reported previously.

The surface of 43040A in the HRSEM micrograph in Figure 3 reveals a porous structure with pore radii ranging from 37 to 185 Å. The resolution limitations of low voltage HRSEM on uncoated, nonconducting surfaces prevents smaller pores from being resolved distinctly.

**Porosity: Ellipsometry.** The decrease in film thickness,  $t$ , with the increase in cure temperature can be

seen from the ellipsometry results in Table 2. The shrinkage,  $s$ , is defined in eq 3 as the reduction in thickness on cure divided by the initial film thickness following baking at 150 °C. The thickness shrinkage is equal to the volumetric shrinkage, since the area of the film remains constant. The shrinkage is negligible following cure at 300 °C, but becomes significant following cure at 400 °C. The shrinkage following exposure to 430 °C for 40 min is approximately 23%, similar to the volume fraction of porogen (approximately 27%). This suggests that the film collapses during cure, filling in the pores generated by porogen degradation. This significant shrinkage might result in substantially less porosity in the films cured at 430 °C than the volume fraction of porogen added to the oligomer.

$$s = \frac{t_{150} - t}{t_{150}} \times 100\% \quad (3)$$

where  $t_{150}$  is the thickness of the film that only underwent a bake.

In addition to the decrease in film thickness, the index of refraction,  $n$ , decreases with increasing cure temperature, as seen from the ellipsometer results in Table 2. The porosity from the ellipsometer results,  $p_n$ , is calculated using eq 4.<sup>31</sup> The changes in refractive index are relatively small following cures at 330 and 400 °C. The change in refractive index is more significant following cure at 430 °C, indicating a porosity of about 3.5%. The porosity of about 3.5% and volume loss of about 23% is not inconsistent with the original porogen content of approximately 27%. The results for 430A are somewhat different from those of the other films cured at 430 °C. The exceptional nature of 430A will be explored further in this paper.

$$p_n = \left( 1 - \frac{(n^2 - 1) \left( \frac{n_{150}^2 + 2}{n_{150}^2 - 1} \right)}{n^2 + 2} \right) \times 100\% \quad (4)$$

where  $n_{150}$  is the refractive index of the film that only underwent a bake.

The self-consistency of the ellipsometer results notwithstanding, an unstated assumption has been made. Using eq 4 assumes that the index of refraction of the porogen-filled oligomer is the same as the index of refraction of a dense (nonporous) polymer following the curing process. Given the two-phase nature of the porogen-filled oligomer, this may not be the case. XRR provides a method of characterizing the porosity without making this assumption.

**Porosity: X-ray Reflectivity.** XRR profiles in a vacuum for the porogen-filled oligomer (150A), for incomplete porogen degradation (400A) and for complete porogen degradation (43040A) are shown in Figure 4. The critical edge,  $q_c$ , which is the  $q_z$  value at the sharp drop in  $\log(I/I_0)$  from the initially flat reflectivity curve, is quite clear in each case. The data were fit to find  $q_c^2$ , which was then used to calculate the electron density. For the materials with a known atomic composition (150, 430, 43040), the electron density was used to calculate the effective mass density,  $d_{\text{eff}}$ .<sup>2-4</sup> The porosity,  $p_V$ , calculated using eq 5 (mass balance), is based on the results from XRR in a vacuum. The  $q_c^2$ ,  $d_{\text{eff}}$ , and  $p_V$  are listed in Table 3.

$$d_{\text{eff}} = d(1 - p_V) \quad (5)$$

where  $d$  is the density of the dense (nonporous) wall material.

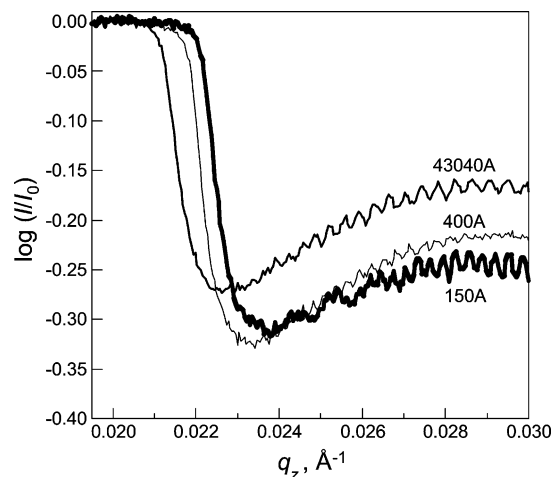


Figure 4. XRR in a vacuum for various cure temperatures.

Table 3. Porosity from XRR in a Vacuum<sup>a</sup>

sample	$q_c^2, \text{Å}^{-2} \times 10^4$	$d_{\text{eff}}, \text{g/cm}^3$	$p_V, \%$
43040A	4.57	1.019	13.6
430A	4.75	1.060	10.2
430B	4.60	1.026	13.1
150A	4.98	1.120	

<sup>a</sup> Uncertainties are discussed in the text.

The critical edge (Figure 4 and Table 3) decreases with increasing processing temperature, indicating a decrease in film density. The effective density of 150A is 1.12 g/cm<sup>3</sup>, close to the density of 1.15 g/cm<sup>3</sup> in Table 1 that was calculated by assuming a density of 1.18 g/cm<sup>3</sup> for the oligomer. Conversely, the measured  $d_{\text{eff}}$  for 150A and the known molecular structure and porogen density can be used to calculate the density of the oligomer (1.14 g/cm<sup>3</sup>) and recalculate the volume content of porogen (26%). This lower oligomer density has a minimal effect on the oligomer neutron scattering length density ( $2.35 \times 10^{-6} \text{Å}^{-2}$  instead of  $2.37 \times 10^{-6} \text{Å}^{-2}$ ) and on the porogen-oligomer neutron scattering contrast ( $3.32 \times 10^{-6} \text{Å}^{-2}$  instead of  $3.30 \times 10^{-6} \text{Å}^{-2}$ ). The calculated shrinkage during the cure of a 1.14 g/cm<sup>3</sup> oligomer to a 1.18 g/cm<sup>3</sup> dense (nonporous) polymer is only 3% (assuming a negligible mass loss during the curing process). The oligomer to polymer cure is not responsible for the significant shrinkage seen with ellipsometry.

The relatively low effective densities for films cured at 400 and 430 °C (Table 3) indicate the formation of a porous material. As 430A has been found to be an exceptional sample, the results from 430B are also listed in Table 3. Assuming a polymer density of 1.18 g/cm<sup>3</sup> for the materials cured at 430 °C yields a porosity of about 13%. A porosity of about 13% is much greater than the very low porosities calculated from ellipsometry measurements. The porosities of the samples cured at 400 °C could not be determined using XRR in a vacuum since their molecular structures and wall densities are unknown. However, the porosities of such samples can be determined by XRR after filling the pores with a known solvent, as illustrated below.

**Porosity: Solvent Absorption X-ray Reflectivity.** Another way to determine porosity by XRR is to measure the electron density of the film before and after the pores are filled with a solvent. The pores are filled through capillary condensation during exposure to saturated vapor. If all of the pores are assumed to fill

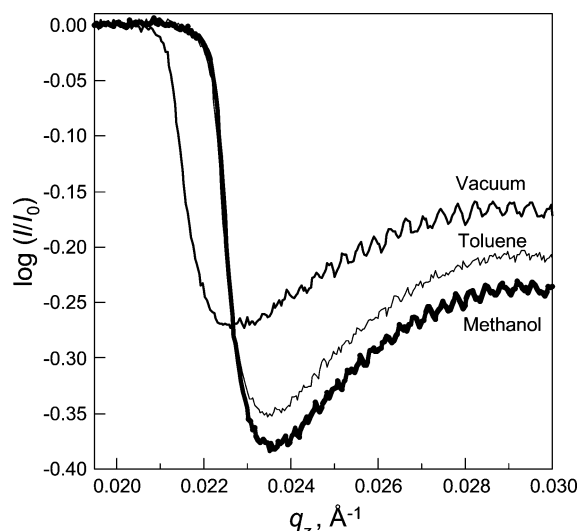


**Figure 5.** XRR of 43040A in a vacuum, methanol vapor and toluene vapor.

**Table 4. Density and Porosity from Solvent Adsorption XRR<sup>a</sup>**

	methanol		toluene	
	$p_M$ , %	$d_M$ , g/cm <sup>3</sup>	$p_T$ , %	$d_T$ , g/cm <sup>3</sup>
43040A	12.1	1.16	9.9	1.13
43040B	9.5	1.16	8.7	1.15
430A	7.9	1.15	7.5	1.15
430B	11.1	1.15	9.9	1.14
400A	5.5		5.2	
400B	4.2		3.2	

<sup>a</sup> Uncertainties are discussed in the text.

with solvent, then the measured volume fraction of solvent in the film is equated with the porosity. The density of the liquid in the pores is assumed to be its bulk density, which is generally a valid assumption provided that the pore diameter is much larger than the size of a solvent molecule. As the porosity is calculated from the change in  $q_c^2$  on filling the pores, the wall density need not be known.<sup>2-4</sup> The increase in  $q_c^2$  on exposure of 43040A to either methanol or toluene is shown in Figure 5. The XRR results in a vacuum are not affected by the exposure of the film to solvents. Samples 430A and 400A exhibit similar changes in their XRR curves following exposure to solvent vapor. The porosities calculated from solvent adsorption XRR with methanol,  $p_M$ , or with toluene,  $p_T$ , are listed in Table 4.

The similarities in the measured porosities using methanol and toluene indicate that in both cases the solvents have penetrated the film and have filled the pores. The porosities measured using solvent-adsorption XRR are somewhat smaller than those in Table 3 based on XRR in a vacuum. There are several possible explanations for the differences in these results. These differences may result from the experimental uncertainty. A wall density of 1.18 g/cm<sup>3</sup> was assumed in the calculations for Table 3. The difference between the two porosity calculations may result if the actual density is slightly different than the assumed density. The results from solvent-adsorption XRR can be used to calculate the density of the wall material if its atomic composition is known. The atomic composition is used to calculate  $d_{\text{eff}}$  from vacuum XRR and then  $p_M$  or  $p_T$  is substituted for  $p_V$  in eq 5. The wall material densities based on the measured porosities from solvent-adsorption XRR are listed in Table 4 ( $d_M$  for methanol,  $d_T$  for toluene). The

density of the polymer calculated in this manner is approximately 1.15 g/cm<sup>3</sup>. Here again, the result is within the limits of experimental uncertainty.

Another possible explanation for the lower porosities obtained from solvent-adsorption XRR is that the wall material swells on exposure to the solvents. Swelling would reduce the density of the wall material and produce an underestimation of the porosity. Initially, the experimental evidence indicated that the wall material did not swell. XRR data for the porogen-filled oligomer films in the presence of either methanol or toluene vapors were identical to XRR data in a vacuum. Exposure of 150A to these solvents did not produce the shift in  $q_c^2$  that would be expected from a reduction in density due to swelling. On the other hand, the porosities in Table 4 from XRR in methanol vapor are slightly greater than those from XRR in toluene vapor. This trend is consistent with swelling, since the swelling would be more extensive from exposure to toluene.

In cases where the films have very smooth surfaces (<10 Å roughness), a high-resolution reflectometer such as the one employed in this study can be used to accurately measure film thickness. Unfortunately, in most cases the relatively thick and rough films did not yield XRR fringes that could be used to produce a reliable estimate of thickness. However, there was one film (400B) for which it was possible to determine film thickness in a vacuum, in methanol vapor and in toluene vapor. In this case, there was a 9% increase in thickness upon exposure to methanol and a 25% increase in thickness upon exposure to toluene. The porosity can be recalculated from the XRR data by using eq 6, which is based on a material balance that assumes that there is only swelling in the thickness direction:

$$p_S = 1 - r_t + \frac{(r_t \rho_{e,\text{swollen}} - \rho_{e,\text{vacuum}})}{\rho_{e,\text{solvent}}} \quad (6)$$

where  $p_S$  is the porosity taking the swelling into account, and  $\rho_{e,\text{swollen}}$ ,  $\rho_{e,\text{vacuum}}$ , and  $\rho_{e,\text{solvent}}$  are the electron densities of the swollen sample, the dry sample, and the solvent, respectively. The extent of swelling,  $r_t$ , is the ratio of the swollen thickness to the original thickness.

Assuming that 43040A swells in a similar fashion, the effects of swelling on the calculation of porosity can be estimated using eq 6. The resulting porosities are 12.6% (instead of 12.1%) from exposure to methanol and 10.3% (instead of 9.9%) from exposure to toluene. Judging by these calculations, the effects of swelling do not produce significant errors in the calculated porosities.

The porosity of the samples cured at 400 °C cannot be calculated using XRR in a vacuum alone since the atomic composition of the wall material is unknown. The results in Table 4, from a combination of XRR in a vacuum and XRR on exposure to solvents, indicate a porosity of about 4.6%, less than half the porosity of the samples cured at 430 °C for 40 min. Assuming swelling, as described above, would yield a porosity of about 7.9%. These results confirm that while there has been significant porogen degradation and pore formation upon exposure to 400 °C, the pore formation process is not yet complete. The error made by assuming no swelling becomes more significant as the porosity decreases.

**Variations in Neutron Scattering with the Extent of Cure.** The SANS data (8 m, 12 Å) for all the materials in set B are presented in Figure 6. All the SANS curves from set B and all the SANS curves from

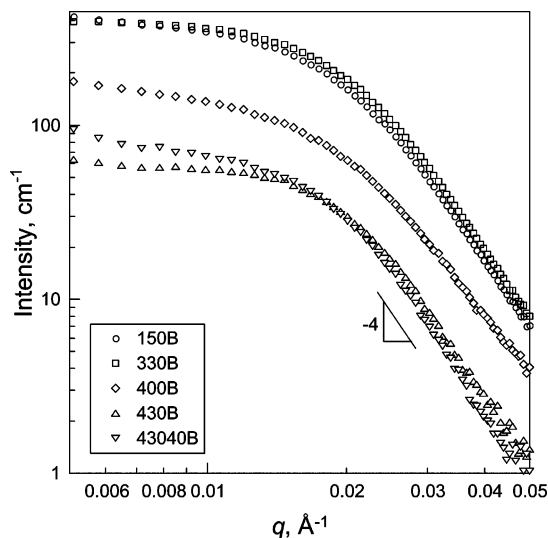


**Figure 6.** SANS of various materials from set B (8 m, 12 Å).

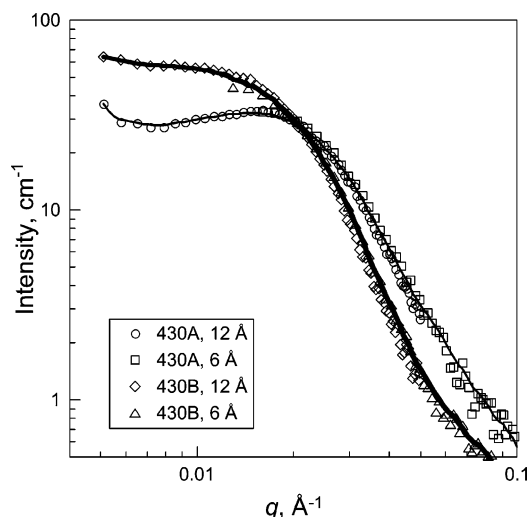


**Figure 7.** SANS of 430A and 430B (8 m, 12 and 6 Å).

set A, except 430A, have similar shapes. The scattering intensities exhibit a plateau below  $q = 0.01 \text{ \AA}^{-1}$  and  $q^{-4}$  scaling behavior above  $q = 0.02 \text{ \AA}^{-1}$ . The similarities in the SANS curves indicate that the two-phase structure of the porogen-filled oligomer is similar to the two-phase structure of the porous polymer. The scattering intensity in Figure 6 progressively decreases, from that for the uncured material (150B and 330B), to that for the material cured at 400 °C, to that for the material cured at 430 °C (430B and 43040B). There are two reasons for the decrease in the scattering intensity. The scattering contrast between the deuterated porogen and the matrix (150B) is greater than that between the pores and the matrix (430B). The amount of porogen in the system decreases with the increase in curing temperature and this reduction in contrast correspondingly reduces the scattering intensity. In addition, scattering intensity decreases due to the reduction in the (pore/porogen) volume fraction during curing from approximately 26% porogen in the oligomer to approximately 12% pores in the polymer.

The high degree of overlap between the midrange data (8 m, 12 Å) and the high range data (8 m, 6 Å), as seen in the SANS curves for 430A and 430B in Figure 7, exists for all the SANS data. There are significant differences in the shapes of the SANS curves for 430A

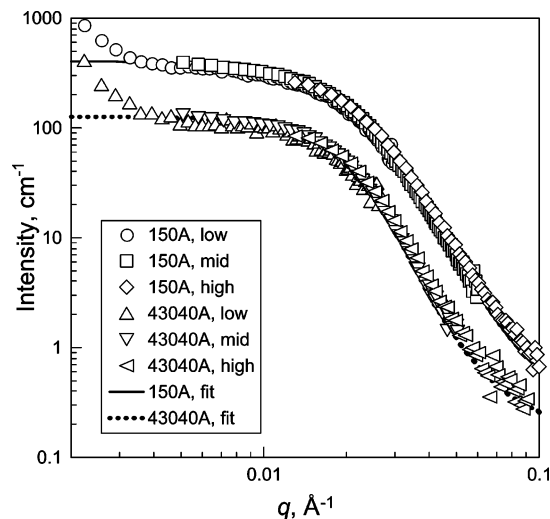


**Figure 8.** SANS of 150A and 43040A (8 m, 12 Å and 6 Å; 30 m, 6 Å) with typical PHS model fits.

and 430B in Figure 7 (the lines connecting the data are included as an aid to the reader). The shape of the SANS curve for 430B is typical of the other samples (a plateau below  $q = 0.01 \text{ \AA}^{-1}$  and  $q^{-4}$  scaling behavior above  $q = 0.02 \text{ \AA}^{-1}$ ). Sample 430A, however, is the one exception to the typical shape exhibited by these SANS curves. Below  $q = 0.01 \text{ \AA}^{-1}$ , the 430A SANS curve exhibits significantly less scattering than 430B. Above  $q = 0.02 \text{ \AA}^{-1}$ , the 430A SANS curve exhibits  $q^{-3}$  scaling behavior, as opposed to the  $q^{-4}$  behavior for 430B. The more rapid decrease in scattering with  $q$  for 430B ( $q^{-4}$  behavior) produces the intersection of the curves seen in Figure 7. These significant differences in the SANS curve for 430A indicate that the architectural arrangement of the two phases is significantly different from those in the other materials.

**The Polydisperse Hard Sphere Model.** The 150A and 43040A SANS data for the low (30 m, 6 Å), mid (8 m, 12 Å) and high (8 m, 6 Å)  $q$  ranges are seen in Figure 8. There is a high degree of overlap in the SANS data for all three  $q$  ranges; the match in the data sets is extraordinarily good. The pore size was estimated by fitting the midrange data to a structural model describing the scattered intensity from a population of polydisperse hard spheres.<sup>37,38</sup> The polydisperse hard sphere (PHS) model includes hard sphere interactions between the particles and uses a Schultz distribution to describe the polydispersity of the radii. The lines in Figure 8 result from a typical fit to the midrange SANS data. The PHS model produces a relatively poor fit of the 430A SANS data. The inability of this structural model to fit the SANS data confirms that the two-phase structure of 430A is, indeed, different from those of the other materials.

The midrange data reach a plateau at low  $q$  that is well described by the PHS model, as shown by the line in Figure 8. The mid- and high-range data are well described by the PHS model. The low range data, however, exhibit an upturn in intensity at very low  $q$  that cannot be described by the PHS model. This upturn in the scattering at very low  $q$  reflects scattering from the micrometer size scale, the scale of the film thickness, and does not reflect the structure at the nanometer size scale. The Debye–Anderson–Brumberger (DAB) structural model,<sup>39</sup> which is based upon the Debye equation<sup>40</sup> and has been used successfully to describe neutron

scattering from some porous low- $k$  materials,<sup>17</sup> was not able to produce good fits to the scattering from these materials.

The PHS model incorporates five fitting parameters: mean pore radius  $R$ , polydispersity PD, volume fraction of a second phase  $v_2$  (the porogen, prior to pyrolysis or the pores, following pyrolysis), scattering contrast SC, and background scattering intensity  $B$ , among which four parameters are independent. The scattering contrast, SC, and the volume fraction of the second phase,  $v_2$ , are dependent parameters. In the fitting process, at least one of  $v_2$  or SC must be fixed while the other may be allowed to vary. Sets of fits were produced by fixing  $v_2$  at values between 0.04 and 0.32 and finding the best fits for SC, the average radius of the dispersed phase,  $R$ , and the polydispersity, PD (PD =  $s/R$ , where  $s^2$  is the variance of the distribution). The background scattering (scattering at high  $q$ ),  $B$ , used in the PHS model was fixed at the experimental data's  $q$ -independent scattering intensity value at high  $q$ .

The  $R$ , PD, and SC values generated by using the model with various  $v_2$  values are seen in Figure 9 for 150A, 400A, and 43040A. The PHS model clearly distinguishes between the size of the porogen domains in 150A and the size of the pores in 43040A (Figure 9). The average radius of the porogen domains is between 55 and 60 Å, depending on  $v_2$ , while the average radius of the pores ranges from 79 to 85 Å. The variation in the radii from the PHS fits for various  $v_2$  is much smaller than the gap between the curves for 150A and 43040A in Figure 9a. The PHS model plainly indicates that, on average, the pores are significantly larger than the porogen domains. Similar conclusions can be drawn for the relatively small variation of PD with  $v_2$  in Figure 9b as compared to the gap between the curves for 150A and 43040A (although the gap for PD is not as large as that for  $R$ ). The PHS model plainly indicates that the breadth of the porogen domain radius distribution is greater than the breadth of the pore radius distribution.

This set of fits can also be used to compare the results of a fit that assumes a specific SC to the results of a fit that assumes a specific  $v_2$ . As  $v_2$  and SC are dependent parameters in the PHS model, SC decreases as  $v_2$  increases (Figure 9c). Here, again, there is no overlap in the SC curves for 150A and 43040A. The PHS model clearly indicates that the porogen-oligomer scattering contrast is significantly larger than the pore-polymer scattering contrast. This observation is consistent with the SLD calculations. In summary, the PHS model clearly indicates that the porogen domains in 150A have a smaller average radius, a broader radius distribution and a higher scattering contrast than the pores in 43040A. A more exact description of the distributions in 150A and 43040A can only be made by assuming specific values for either  $v_2$  or SC. This approach will be explored further in this paper.

The structure of the film cured at 400 °C is quite different from the two-phase structure upon which the PHS model is based. The porogen has not completely degraded following a cure at 400 °C. There are at least three phases in 400A: the incompletely degraded porogen, the partially cured oligomer, and the pores. This three-phase structure produces a complex scattering system. The application of the PHS model to the 400A SANS data can only produce a description of a two-phase structure that would produce identical scattering.

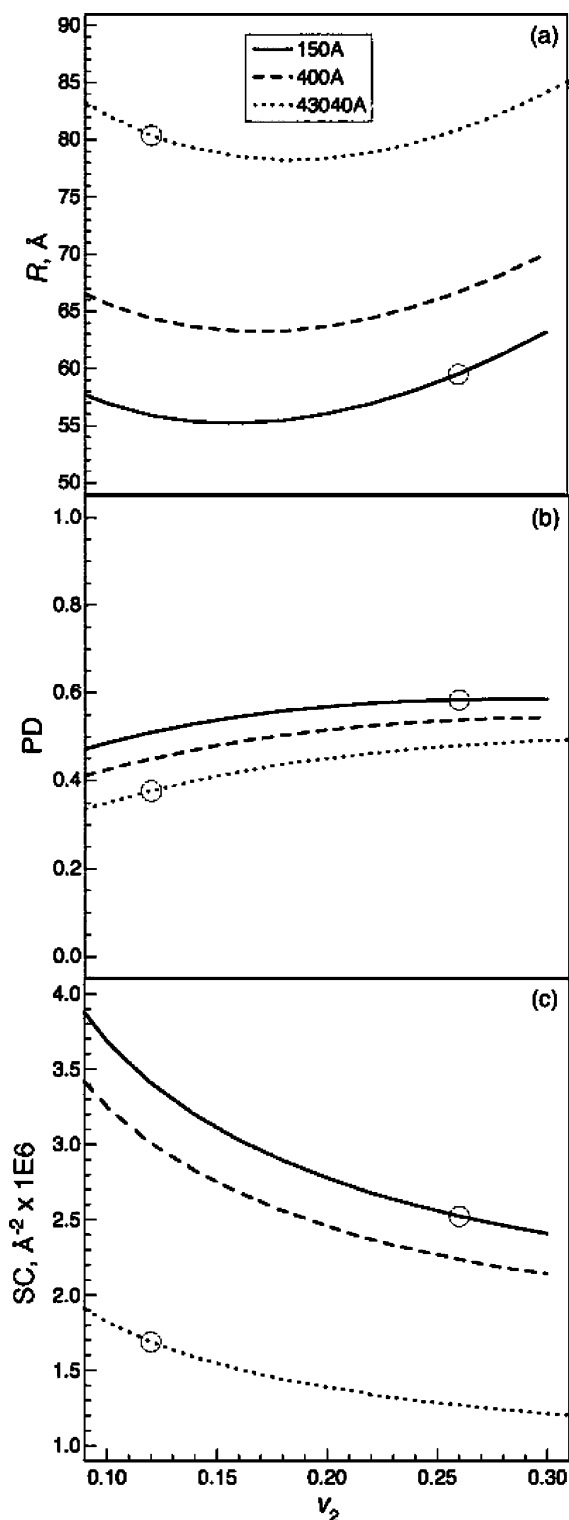


**Figure 9.** (a)  $R$ , (b) PD, and (c) SC from the PHS fits to the 150A, 400A and 43040A SANS data: variation with  $v_2$ . The circles indicate the values assuming a  $v_2$  of 0.26 for 150A and 0.12 for 43040A.

The set of fits resulting from applying the PHS model to the SANS data from 400A is seen in Figure 9. As expected, the SC curve in Figure 9c for the two-phase system “equivalent” to 400A lies between those for 150A and 43040A. 400A contains both porogen and pores and its SC is expected to lie between those of the porogen-oligomer system and the pore-polymer system. The narrow  $R$  range for the 400A-equivalent two-phase system clearly lies between those for 150A and 43040A

**Table 5. Results from PHS Fits to the SANS Data Using a Reasonable  $v_2$** 

sample	$R$ , Å (fit)	PD (fit)	$v_2$ (fixed)	SC, Å <sup>-2</sup> × 10 <sup>6</sup> (fit)	$B$ , cm <sup>-1</sup> (fixed)
150A	60	0.58	0.26	2.5	0.30
150B	64	0.57	0.26	2.5	0.40
330A	78	0.46	0.26	2.6	0.40
330B	77	0.45	0.26	2.7	0.30
430B	85	0.29	0.1	1.4	0.35
43040A	80	0.38	0.12	1.7	0.20
43040B	70	0.46	0.12	1.3	0.25

in Figure 9a. Similarly, the PD range for the 400A-equivalent two-phase system clearly lies between those for 150A and 43040A in Figure 9b. This approach can describe an unknown structure using a small range of fit results that are based on a reasonable range of parameters.

**Polydisperse Hard Sphere Model: Fixed  $v_2$ .** A  $v_2$  of 0.26 for the porogen–oligomer system is an obvious choice. A  $v_2$  of 0.12 for the materials exposed to 430 °C was chosen as representative. The  $R$ , PD, and SC obtained using these fixed  $v_2$  are listed in Table 5 and are marked with circles on the curves for 150A and 43040A in Figure 9. The  $R$  and PD generated using these  $v_2$  confirm the trends observed from Figure 9. The porogen domains have a smaller average radius (60 Å for 150A) and a wider polydispersity (0.58 for 150A) while the pores have a larger average radius (80 Å for 43040A) and a narrower polydispersity (0.38 for 43040A).

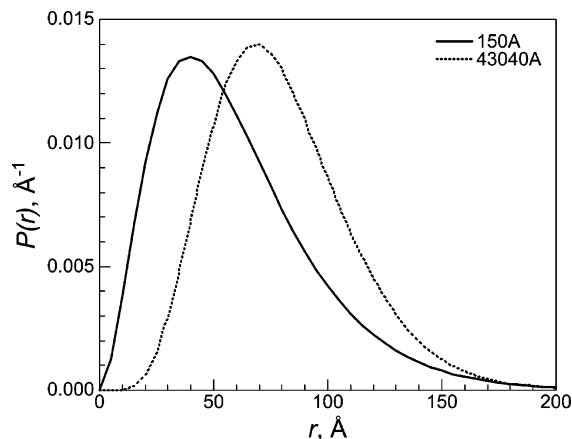
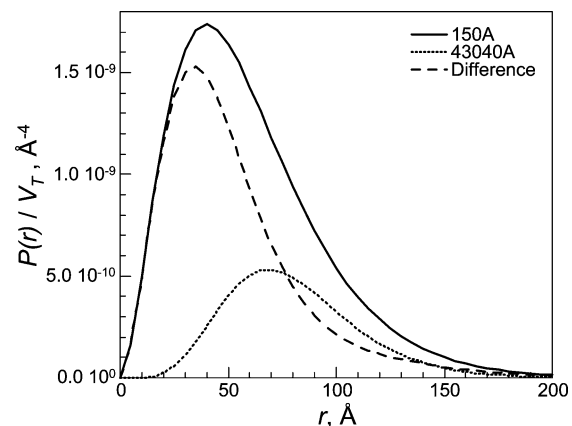
The porogen domain size distribution and the pore size distribution can be plotted by substituting the  $R$  and PD from Table 5 into the Schulz distribution (eq 7).<sup>37,38,41</sup> The width of the distribution,  $z$ , can be calculated using eq 8. The integral of the area under the probability distribution curves generated using eq 7 is 1.0. The general shapes of the Schulz distribution curves for 150A and 43040A in Figure 10 are similar. The differences in the distributions, reflected in the different  $R$  and PD in Table 5, can be seen through a comparison of the curves.  $P(r)$  for 150A has a significant population of porogen domains at lower  $r$  that is not present in the pores in 43040A.  $P(r)$  for 43040A has a significant population of pores at higher  $r$  that is not present in the porogen domains in 150A. The maximum in  $P(r)$  for 43040A in Figure 10 is about 30 Å greater than the maximum in  $P(r)$  for 150A. In addition,  $P(r)$  for 150A in Figure 10 is somewhat broader than  $P(r)$  for 43040A.

$$P(r) = \frac{1}{\Gamma(z+1)} \left(\frac{z+1}{R}\right)^{z+1} r^z \exp\left(-\left(\frac{z+1}{R}\right)r\right) \quad (7)$$

$$PD = \frac{1}{\sqrt{z+1}} = \frac{s}{R} \quad (8)$$

where  $r$  is the radius and  $\Gamma$  is the gamma function.

The differences between the porogen domain distribution in 150A and the pore distribution in 43040A can be better described by taking both the different size distributions and the different volume fractions into account. The total volume of the porogen or pores described by  $P(r)$ ,  $V_P$ , can be calculated through integration (eq 9). The total sample volume,  $V_T$ , can be calculated by dividing  $V_P$  by the porogen or pore volume fraction,  $v_2$ . The Schulz distributions normalized by the total sample volumes,  $P(r)/V_T$ , are presented in Figure 11. In this manner, the number of pores of a specific size within a unit volume can be compared

**Figure 10.**  $P(r)$  from Schulz distributions for 150A and 43040A based on the PHS model results.**Figure 11.**  $P(r)$  from Schulz distributions for 150A and 43040A based on the PHS model results normalized by the total sample volume  $V_T$  based on the 0.26 porogen  $v_2$  in 150A and the 0.12 pore  $v_2$  in 43040A.

to the number of porogen domains of the same size within the same unit volume.

$$V_P = \int_0^{\infty} \frac{4}{3}\pi r^3 P(r) dr \quad (9)$$

Visual inspection of the curves in Figure 11 provides more insight into the pore formation process. The coincidence of the curves for 150A and 43040A in Figure 11 is greater at relatively large radii. This seems to indicate that relatively large porogen domains degrade to form relatively large pores. The large number of relatively small porogen domains do not form small pores. The distribution of the porogen domains that do not become pores is shown by the curve that represents the difference between the curves for 150A and 43040A. The difference curve indicates that the large number of small porogen domains vanishes during cure. The relatively small porogen domains have a higher interfacial tension and would be more prone to collapse during porogen degradation. The disappearance of the larger domains is not as significant, number-wise. However, evaluating the data in terms of volume fractions (not shown) has indicated that the disappearance of the large domains is significant volume-wise. The collapse of the porogen domains during degradation yields the reduction in film thickness, the reduction in the dispersed phase volume fraction, and the reduction in the distribution's breadth.

**Polydisperse Hard Sphere Model: Fixed SC.**

There is, however, one significant problem using a  $v_2$  of 0.26 for the materials exposed to 150 °C and 330 °C and a  $v_2$  of 0.12 for the materials exposed to 430 °C. The porogen-oligomer SC that results from using the PHS model is approximately  $2.6 \times 10^{-6} \text{ \AA}^{-2}$ , significantly less than the calculated value of  $3.30 \times 10^{-6} \text{ \AA}^{-2}$ . The relatively low scattering contrast from the PHS fit could, perhaps, be explained by porogen-oligomer interdiffusion that reduces the scattering. However, the polymer-pore SC that results from using the PHS model (approximately  $1.6 \times 10^{-6} \text{ \AA}^{-2}$ ) is also significantly less than the calculated value ( $2.37 \times 10^{-6} \text{ \AA}^{-2}$ ). There are significant discrepancies between the SC values from the SLD calculations that were based on molecular structures and densities and the SC values from the PHS model fits that used reasonable values of  $v_2$ . These discrepancies may indicate that there are significant differences between the structure of the films and the structure upon which the PHS model is based.

In light of these discrepancies in SC, an alternate approach to the PHS model was used. The SC was fixed to the calculated value and the PHS model was used to find  $v_2$ ,  $R$  and PD from the best fit to the SANS data ( $B$  was fixed as described previously). As can be expected from the variation of SC with  $v_2$  in Figure 9c, using a significantly higher SC yields a significantly lower  $v_2$ . Unfortunately, the low volume fractions generated using this approach do not correspond well to known porogen volume fractions and measured porosities. The PHS fit to the scattering from 150A using an SC of  $3.30 \times 10^{-6} \text{ \AA}^{-2}$  yields a  $v_2$  of 0.12, much lower than expected from a porogen volume content of 26%. This fit also yields an  $R$  of 56 Å and a PD of 0.51. The PHS fit to the scattering from 43040A using an SC of  $2.37 \times 10^{-6} \text{ \AA}^{-2}$  yields a  $v_2$  of 0.06, much lower than the 0.12 expected from the XRR results. The fit also yields an  $R$  of 87 Å and a PD of 0.29. The  $R$  and PD values for 150A and 43040A produced by fixing SC are quite similar to those in Table 5 produced by fixing  $v_2$ . This approach yields the same description of the changes in structure on porogen degradation, the average radius of the discrete phase becomes larger and the radius distribution becomes narrower. It is also interesting to note that the resulting 43040A:150A  $v_2$  ratio, 0.06:0.12, is similar to the ratio based on the assumed  $v_2$  values.

Using the known  $v_2$  in the PHS model yields an SC that is smaller than the expected value, while using the calculated value of SC yields a  $v_2$  that is smaller than the expected value. Despite these contradictions, the PHS model does provide a relatively clear description of the structural changes that take place during porogen degradation and pore formation: the smaller porogen domains collapse while the larger porogen domains form pores. These structural changes are consistent with the observed reduction in thickness and the relatively low porosity, providing a clear description of the porogen degradation and pore formation processes in these materials.

**Conclusions**

The combination of XRR and SANS is a powerful tool for describing porogen degradation and pore formation in nanoporous materials. The porosity in systems with an unknown wall material can be determined using solvent absorption XRR. Insight into the pore formation process can be obtained through the use of a deuterated

porogen. The SANS data from such systems can be interpreted using the polydisperse hard sphere model. Several specific conclusions may be drawn regarding the nanoporous polyphenylene material investigated:

The acetylene groups reacted during the cure process. The simultaneous cure and porogen degradation produced an ether-containing hydrocarbon residue.

Only pores of 37 Å and greater could be directly observed by HRSEM due to the resolution limitations associated with uncoated, nonconducting surfaces.

The oligomer contained 26 vol % porogen domains having a relatively broad size distribution whose average radius was approximately 60 Å.

The porogen degraded on exposure to elevated temperatures. This degradation was incomplete at 400 °C. During degradation, the smaller porogen domains collapsed, while the larger porogen domains yield stable pores.

The collapse of a large number of relatively small pores produced a significant reduction in film thickness, a porosity that was significantly smaller than the porogen content, a pore size distribution that was narrower than the porogen domain size distribution and an average pore size of approximately 80 Å.

An analysis of the SANS results demonstrated that the material 430A, which exhibited atypical ellipsometry and XRR results, had a two-phase structure that was different from those of the other materials.

**Acknowledgment.** The authors gratefully acknowledge the inimitable assistance of Derek L. Ho and Charles J. Glinka, Center for Neutron Research, National Institute of Standards and Technology. We acknowledge the support of the National Institute of Standards and Technology, US Department of Commerce, in providing the neutron research facilities used in this work. M.S.S. would like to thank the National Institute of Standards and Technology for their generous support.

**References and Notes**

- (1) *International Technology Road map for Semiconductors, 2004 Update*; Semiconductor Industry Association, San Jose, CA, 2004.
- (2) Bauer, B.; Lin, E. K.; Lee, J. J.; Wang, H.; Wu, W. L. *J. Electron. Mater.* **2001**, *30*, 304.
- (3) Lee, H. J.; Lin, E. K.; Wu, W. L.; Fanconi, B. M.; Lan, J. K.; Cheng, Y. L.; Liou, H. C.; Wang, Y. L.; Feng, M. S.; Chao, C. G. *J. Electrochem. Soc.* **2001**, *148*, F195.
- (4) Lee, H. J.; Soles, C. L.; Liu, D. W.; Bauer, B. J.; Wu, W. L. *J. Polym. Sci., Part B: Polym. Phys.* **2002**, *40*, 2170.
- (5) Lee, H. J.; Soles, C. L.; Liu, D. W.; Bauer, B. J.; Wu, W. L. *Polym. Mater.: Sci. Eng.* **2002**, *87*, 435.
- (6) Wu, W. L.; Wallace, W. E.; Lin, E. K.; Lynn, G. W.; Glinka, C. J.; Ryan, E. T.; Ho, H. M. *J. Appl. Phys.* **2000**, *87*, 1193.
- (7) Silverstein, M. S.; Bauer, B. J.; Lee, H. J.; Hedden, R. C.; Landes, B.; Lyons, J.; Kern, B.; Niu, J.; Kalantar, T. In *Characterization and Metrology for ULSI Technology 2003*; Seiler, D. G., Diebold, A. C., Shaffner, T. J., McDonald, R., Zollner, S., Khosla, R. P., Secula, E. M., Eds.; AIP Conference Proceedings 683; AIP: New York, 2003; p 572.
- (8) Baklanov, M. R.; Mogilnikov, K. P.; Polovkinkin, V. G.; Dultsev, F. N. *J. Vac. Sci. Technol. B* **2000**, *18*, 1385.
- (9) Shamiryan, D. G.; Baklinov, M. R.; Vanhaelemeersch, S.; Maex, K. *Electrochem. Solid State Lett.* **2001**, *4*, F3.
- (10) Murray, C.; Flannery, C.; Steiner, I.; Schulz, S. E.; Baklinov, M. R.; Mogilnikov, K. P.; Himcinschi, C.; Friedrich, M.; Zahn, D. R. T.; Gessner, T. *Microelectron. Eng.* **2002**, *60*, 133.
- (11) Baklinov, M. R.; Mogilnikov, K. P. *Microelectron. Eng.* **2002**, *64*, 335.
- (12) Mogilnikov, K. P.; Baklinov, M. R. *Electrochem. Solid State Lett.* **2002**, *5*, F29.

- (13) Baklinov, M. R.; Mogilnikov, K. P.; Yim, J. H. *Mater. Res. Soc. Symp. Proc.* **2004**, *812*, F5.4.1.
- (14) Lee, H. J.; Soles, C. L.; Liu, D. W.; Bauer, B. J.; Lin, E. K.; Wu, W. L.; Grill, A. *J. Appl. Phys.* **2004**, *95*, 2355.
- (15) Soles, C. L.; Lee, H. J.; Lin, E. K.; Wu, W. L. *Pore Characterization in Low-k Dielectric Films Using X-ray Reflectivity: X-ray Porosimetry*, NIST: Washington, DC, 2004.
- (16) Lin, E. K.; Lee, H. J.; Lynn, G. W.; Wu, W. L.; O'Neill, M. L. *Appl. Phys. Lett.* **2002**, *81*, 607.
- (17) Hedden, R. C.; Lee, H. J.; Bauer, B. *Langmuir*, **2004**, *20*, 416.
- (18) Hedden, R. C.; Bauer, B.; Lee, H. J. *Mater. Res. Soc. Symp. Proc.* **2003**, *766*, E9.7.1.
- (19) Hedden, R. C.; Lee, H. J.; Soles, C. L.; Bauer, B. *Polym. Mater.: Sci. Eng.* **2004**, *90*, 494.
- (20) Bauer, B. J.; Hedden, R. C.; Lee, H. J.; Soles, C. L.; Liu, D. W. *Mater. Res. Soc. Symp. Proc.* **2003**, *766*, E8.9.1.
- (21) Gidley, D. W.; Frieze, W. E.; Dull, T. L.; Sun, J.; Yee, A. F.; Nguyen, C. V.; Yoon, D. Y. *Appl. Phys. Lett.* **2000**, *76*, 1282.
- (22) Sun, J. N.; Gidley, D. W.; Dull, T. L.; Frieze, W. E.; Yee, A. F.; Ryan, E. T.; Lin, S.; Wetzell, J. *J. Appl. Phys.* **2001**, *89*, 5138.
- (23) Ro, H. W.; Kim, K. J.; Theato, P.; Gidley, D. W.; Yoon, D. Y. *Macromolecules* **2005**, *38*, 1031.
- (24) Huang, Q. R.; Volksen, W.; Huang, E.; Toney, M.; Frank, C. W.; Miller, R. D. *Chem. Mater.* **2002**, *14*, 3676.
- (25) Omote, K.; Ito, Y.; Kawamura, S. *Appl. Phys. Lett.* **2003**, *82*, 544.
- (26) Kim, H. C.; Volksen, W.; Miller, R. D.; Huang, E.; Yank, G.; Briber, R. M.; Shin, K.; Satija, S. K. *Chem. Mater.* **2003**, *15*, 609.
- (27) Kondoh, E.; Baklanov, M. R.; Lin, E.; Gidley, D.; Nakashima, A. *Jpn. J. Appl. Phys.* **2001**, *40*, L323.
- (28) Martin, S. J.; Godschalx, J. P.; Mills, M. E.; Shaffer, E. O.; Townsend, P. H. *Adv. Mater.* **2000**, *12*, 1769.
- (29) Posseme, N.; Chevolleau, T.; Joubert, O.; Vallier, L.; Mangiagalli, P. *J. Vac. Sci. Technol. B* **2003**, *21*, 2432.
- (30) Yang, S.; Mirau, P.; Sun, J.; Gidley, D. W. *Radiat. Phys. Chem.* **2003**, *68*, 351.
- (31) Maex, K.; Baklanov, M. R.; Shamiryn, D.; Iacopi, F.; Brongersma, S. H.; Yanovitskaya, Z. S. *J. Appl. Phys.* **2003**, *93*, 8793.
- (32) Maier, G. *Prog. Polym. Sci.* **2001**, *26*, 3.
- (33) Strittmatter, R. J.; Hahnfeld, J. L.; Silvis, H. C.; Stokich, T. M.; Perry, J. D.; Ouellette, K. B.; Niu, Q. J.; Godschalx, J. P.; Kalantar, T. H.; Mubarekyan, E.; Hefner, R. E.; Lyons, J. W.; Dominowski, J. M.; Buske, G. R. *Mater. Res. Soc. Symp. Proc.* **2003**, *766*, E7.5.1.
- (34) Mohler, C. E.; Landes, B. G.; Meyers, G. F.; Kern, B. J.; Ouellette, K. B.; Magonov, S. In *Characterization and Metrology for ULSI Technology 2003*; Seiler, D. G., Diebold, A. C., Shaffner, T. J., McDonald, R., Zollner, S., Khosla, R. P., Secula, E. M., Eds.; AIP Conference Proceedings 683; AIP: New York, 2003; p 562.
- (35) Landes, B.; Kern, B.; Stokich, T.; Niu, J.; Yontz, D.; Radler, M.; Mohler, C. E.; Ouellette, K.; Lucero, S.; Hahnfeld, J.; King, D. *Mater. Res. Soc. Symp. Proc.* **2003**, *766*, E9.10.1.
- (36) Ankner, J. F.; Majkrzak, C. F. In *Neutron Optical Devices and Applications*; Majkrzak, C. F., Wood, J. M. Eds.; SPIE Conference Proceedings 1738; SPIE, Bellingham, WA, 1992; p 261.
- (37) Griffith, W. L.; Triolo, R.; Compere, A. L. *Phys. Rev. A* **1986**, *33*, 2197.
- (38) Griffith, W. L.; Triolo, R.; Compere, A. L. *Phys. Rev. A* **1987**, *35*, 2200.
- (39) Debye, P.; Anderson, H. R.; Brumberger, H. *J. Appl. Phys.* **1957**, *28*, 679.
- (40) Roe, R. J. *Methods of X-ray and Neutron Scattering in Polymer Science*, Oxford University Press: New York, 2000.
- (41) Tuinier, R.; Petukhov, A. V. *Macromol. Theory Simul.* **2002**, *11*, 975.

MA047353T